Ocean Systems Engineering, *Vol. 5, No. 3 (2015) 139-160*
DOI: http://dx.doi.org/10.12989/ose.2015.5.3.139

Global performances of a semi-submersible 5 MW wind-turbine including second-order wave-diffraction effects

H.C. Kim*[1] and M.H. Kim[2]

[1]*Texas A&M University, College Station, TX 77843, USA*
[2]*Civil Engineering, Texas A&M University, College Station, TX 77843, USA*

(Received May 17, 2015, Revised August 19, 2015, Accepted August 27, 2015)

Abstract. The global performance of the 5 MW OC4 semisubmersible floating wind turbine in random waves was numerically simulated by using the turbine-floater-mooring fully coupled and time-domain dynamic analysis program FAST-CHARM3D. There have been many papers regarding floating offshore wind turbines but the effects of second-order wave-body interactions on their global performance have rarely been studied. The second-order wave forces are actually small compared to the first-order wave forces, but its effect cannot be ignored when the natural frequencies of a floating system are outside the wave-frequency range. In the case of semi-submersible platform, second-order difference-frequency wave-diffraction forces and moments become important since surge/sway and pitch/roll natural frequencies are lower than those of typical incident waves. The computational effort related to the full second-order diffraction calculation is typically very heavy, so in many cases, the simplified approach called Newman's approximation or first-order-wave-force-only are used. However, it needs to be justified against more complete solutions with full QTF (quadratic transfer function), which is a main subject of the present study. The numerically simulated results for the 5 MW OC4 semisubmersible floating wind turbine by FAST-CHARM3D are also extensively compared with the DeepCWind model test results by Technip/NREL/UMaine. The predicted motions and mooring tensions for two white-noise input-wave spectra agree well against the measure values. In this paper, the numerical static-offset and free-decay tests are also conducted to verify the system stiffness, damping, and natural frequencies against the experimental results. They also agree well to verify that the dynamic system modeling is correct to the details. The performance of the simplified approaches instead of using the full QTF are also tested.

Keywords: wind energy; FOWT (Floating Offshore Wind Turbine); OC4 semi-submersible; dynamic coupling; mooring tension; second order wave diffraction effect; QTF; FAST-CHARM3D; 5 MW wind-turbine; viscous drag

1. Introduction

The importance of more clean renewable energy has been underscored to secure new energy source and protect environments. Especially, wind energy is appealing since it is economically competitive, technologically proven, infinitely renewable, and does not make any waste or carbon

∗Corresponding author, Ph.D. Student, E-mail: doriduul@tamu.edu
[a] Professor, E-mail: m-kim3@tamu.edu

 ISSN: 2093-6702 (Print), 2093-677X (Online)

emission. Recently, several countries installed offshore floating wind turbines (Dominique et al., 2010). Although they are considered to be more difficult to design than fixed offshore wind turbines, floating wind turbines have many advantages compared to onshore or bottom fixed offshore wind turbines. In general, they are less restricted by regulation, with higher-quality wind, and less sensitive to space/size/noise/visual/foundation restrictions. In this regard, if the technology is completely developed, floating offshore wind turbines are expected to be more popular to generate considerable amounts of clean renewable energy at competitive prices compared to other energy sources (Henderson *et al*. 2002, Henderson *et al*. 2004, Musial *et al*. 2004, Tong 1998, Wayman *et al*. 2006).

One of the challenging issues on the floating offshore wind turbine is the coupled dynamics analysis among the mooring system, floating platform, and wind turbine. Therefore, for reliable design, it is necessary to develop the integrated tool to accurately analyze the fully coupled dynamics including control. Some efforts are in progress toward this direction for several selected types of floating offshore wind turbines. In this paper, the global performance analysis of the OC4 5-MW semi-submersible floating wind turbine was conducted by the fully coupled dynamic analysis tool, the combination of FAST (e.g., Jonkman 2004) and CHARM3D (e.g., Yang and Kim 2010, Kang and Kim 2012), developed by the second author's research group (e.g., Bae and Kim 2011, 2014). Previously, NREL organized the Offshore Code Comparison Collaboration (OC4) (Robertson *et al.* 2012) in order to verify the accuracy of offshore wind turbine dynamics simulation codes by comparing results among various numerical tools and against systematically obtained experimental results.

For the OC4 semi-submersible case, Masciola *et al*. (2013) analyzed the system by including only linear wave force and using quasi-static or lumped-mass methods for mooring model. Also, Coulling *et al*. (2013a, b) performed the validation for the semi-submersible platform including second-order wave-diffraction forces based on Newman's approximation. However, the mooring model in the analysis was also quasi-static, so the true dynamic coupling with mooring lines was missing in the study. Besides, the second-order wave-diffraction force was approximated by Newman's approximation method, and thus, there is a need to check the results by using the actual second -order wave-diffraction forces. Recently, Koo *et al*. (2014a) analyzed the OC4 semisubmersible wind turbine and compared their numerical predictions by their own code, MLTSIM-FAST against DeepCWind model test results. Moreover, the second-order wave-diffraction effects were briefly introduced and discussed in their work (Koo *et al*. 2014b). On the other hand, Zhao and Wan carried out motion simulations of the OC4 semi-submersible platform in waves by using their own CFD code, naoe-FOAM-SJTU. (Zhao and Wan 2015).

In this paper, the fully coupled wind-turbine/hull/mooring dynamics of the OC4 semi-submersible model are calculated by including viscous and second-order difference-frequency wave effects with FE(finite element)-based mooring dynamics module. Also, the complete second-order results (Kim and Yue 1989, 1990, 1991) are compared with first-order-wave-force-only results, Newman's approximation results, and DeepCWind model test results (Coulling *et al.* 2013b). The numerically modeled dynamic system was fully identified through the static-offset and free-decay tests. The system was further analyzed for irregular waves represented by white-noise input-wave spectra and the results were validated against experimental results. For the numerical examples shown in this paper, wind and current are not included to reduce the factors of uncertainties in the comparisons between numerical prediction and model test. The turbine-floater-mooring fully coupled dynamic analysis including blade control and wind-wave-current will be the subject of the next study after this kind of initial validation done in

this paper.

2. Numerical simulation in time domain

In order to solve a wind turbine on a single floating platform, FAST (e.g., Jonkman and Buhl Jr. 2004), developed by National Renewable Energy Laboratory (NREL), was modified and extended so that it can calculate the full coupled dynamics among wind turbine, floating platform, and mooring lines. The coupled dynamic response between the turbine and floater can be derived from the full-DOF matrix equation including floater 6-DOFs and additional multi-wind-turbine DOFs with proper platform-turbine coupling terms. The combined left-hand-side matrix with the given forcing functions in the right-hand side is solved at each time step. Assuming that every degree of freedom for a three-bladed turbine in FAST is turned on, the total DOFs can be expressed as 6 (for floater) +19 (for turbine)=25. The coupled terms between the floating platform and turbine in the coefficient matrix can be derived by accounting for every effect of generalized inertia and active forces from both bodies. The detailed theory and equations are given in Bae and Kim (2014)

Between the floater and mooring line dynamics, the necessary data exchange is also done at each time step for their dynamic coupling. The hydro-dynamic loadings and instantaneous tensions for mooring lines are obtained from CHARM3D (e.g., Kim *et al*. 2001, Tahar and Kim 2003, Yang and Kim 2010) along with viscous forces on Morison members and convolution-integral forces for floater. They are fed to FAST at each time step. The transferred external forces include first-order and second-order wave forces. Then FAST fills out the forcing function of the platform DOFs using those transferred forces, and solves displacements, velocities, and accelerations of all the degrees of freedom including elastic responses of towers and blades. The obtained platform displacement and velocity data are then fed into CHARM3D side to update the external forces. The instantaneous velocites of the platform are used for the next-time-step convolution–integral term. The instantaneous positions of the platform's Morison members are used for viscous drag forces with instantaneous incident-wave kinematics. The transferred instantaneous positions of the mooring-connection points are used as an input for the next-time-step mooring dynamics. The basic concept of rotor-floater coupling is schematically shown in Fig. 1.

3. Second-order wave loads and convolution integral in time domain

In this section, the time-domain realization of the first- and second-order wave forces/moments in a random sea environment is explained. The first- and second-order hydrodynamic forces/moments on a body caused by stationary Gaussian random seas can be written as a two-term Volterra series in the time domain as follows

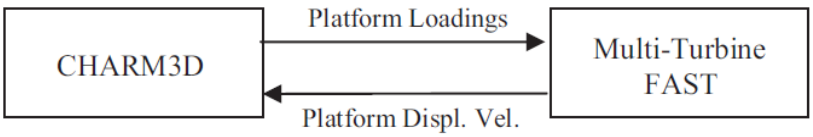

Fig. 1 Basic concept of FAST-CHARM3D coupling

$$F^{(1)}(t) + F^{(2)}(t) = \int_{-\infty}^{\infty} h_1(\tau)\eta(t-\tau)d\tau + \int_{-\infty}^{\infty}\int_{-\infty}^{\infty} h_2(\tau_1,\tau_2)\eta(t-\tau_1)\eta(t-\tau_2)d\tau_1 d\tau_2 \quad (1)$$

Where $\eta(t)$ is the ambient wave free surface elevation at a reference position, $h_1(t)$ is the linear impulse response function, and $h_2(\tau_1,\tau_2)$ is the quadratic impulse response function. The above equation can be expressed in the form of the summation of N frequency component waves as below

$$F_I^{(1)}(t) = Re\left[\sum_{j=1}^{N} A_j L(\omega_j) e^{i\omega t}\right] \quad (2)$$

$$F_I^{(2)}(t) = Re\left[\sum_{j=1}^{N}\sum_{k=1}^{N} A_j A_k^* D(\omega_j, -\omega_k) e^{i\omega^- t}\right] \quad (3)$$

Where $L(\omega_j)$ represents the linear force transfer function (LTF), A is wave amplitude, and $D(\omega_j, -\omega_k)$ is the difference-frequency quadratic transfer functions (QTF). The sum-frequency second-order forces/moments are not included in (3) since they play little role for the overall dynamics of semisubmersible platform. On the other hand, $F_I^{(2)}(t)$ can be rewritten by Newman's approximation as following equation.

$$F_I^{(2)}(t) = Re\left[\sum_{j=1}^{N}\sum_{k=1}^{N} A_j A_k^* D\left(\frac{\omega_j+\omega_k}{2}, \frac{\omega_j+\omega_k}{2}\right) e^{i\omega^- t}\right] \quad (4)$$

The radiation-potential-induced force/moment in time domain can be expressed as follows

$$F_R(t) = -M^a(\infty)\ddot{\zeta}(t) - \int_{-\infty}^{t} R(t-\tau)\dot{\zeta}(\tau)d\tau \quad (5)$$

Where ζ is platform motion, upper dot is time derivative, $M^a(\infty)$ is the added mass of platform at infinite frequency, and $R(t)$ is retardation function or time-memory function, which is related to the frequency-domain solutions of the radiation problem as follows

$$R(t) = \frac{2}{\pi}\int_0^{\infty} C(\omega)\frac{sin\omega t}{\omega} d\omega \quad (6)$$

Where $C(\omega)$ is the radiation-wave-induced damping coefficient at frequency ω.

The total wave loads in time domain can then be written by summing all the force components as below.

$$F_{total}(t) = F_I(t) + F_R(t) \quad (7)$$

where the total wave exciting force $F_I(t) = F_I^{(1)}(t) + F_I^{(2)}(t)$.

4. DeepCWind semisubmersible wind-turbine model description

Table 1 and Fig. 2 show the floating platform properties and DeepCwind offshore wind-turbine geometry, respectively. (Coulling *et al*. 2013) The property in Table 1 is about only the floating platform, and the wind turbine part is not included. The wind turbine is based on NREL 5 MW baseline turbine (Jonkman *et al*. 2007), but it is modified for a 1/50th scale model test. (Coulling *et al*. 2013).

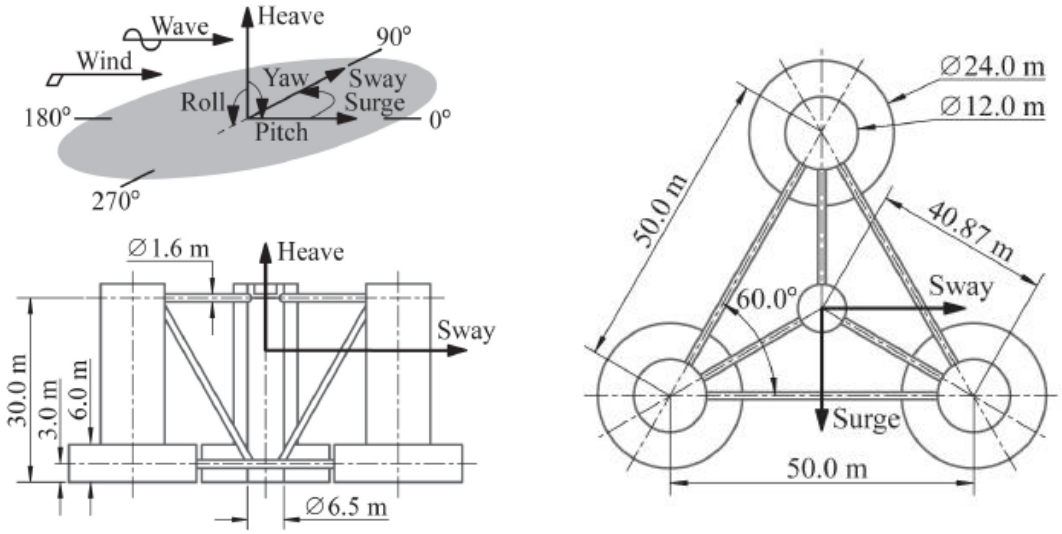

Fig. 2 DeepCwind Semisubmersible platform geometry front view (left) and Top view (right) (Coulling *et al*. 2013)

Table 1 offshore floating platform property

ITEM	Unit	Value
Platform Center of Mass	m	-14.4
Platform Mass	ton	1.3444E+04
Platform Inertia Ixx, Iyy	kg-m^2	8.0110E+09
Platform Inertia Izz	kg-m^2	1.3910E+10
Nacelle and blade Mass	ton	397.1
Tower Mass	ton	302.2

5. Numerical modeling

The x-axis symmetry is used and the half domain is discretized by 3600 panels. Panels near the free surface are more finely modeled as shown in Fig. 3. The convergence test with a finer model was carried out and it was checked that the added mass, radiation damping, and linear- and second-order wave forces were converged satisfactorily for the present application. The potential-based hydrodynamic coefficients and excitations are calculated by WAMIT in a frequency domain, and they are subsequently used for time-domain simulations for FAST-CHARM3D. Also, the viscous force is added using drag-force formula for Morison members i.e., the braces that connect between columns and pontoons are modeled as Morison members. Since the crossflow drag forces are proportional to relative velocities squared, they can contribute both for excitation and damping. The viscous drag forces on members above MWL are

also evaluated at each time step by using the instantaneous wave kinematics extrapolated from the values at MWL. In this study, uniform extrapolation is used for that purpose. The nonlinear viscous drag forces evaluated at instantaneous platform positions also contribute to nonlinear motion components with higher harmonics.

6. Added mass and radiation damping

The added mass and radiation damping can be calculated with the body-surface panels of Fig. 3 by using the first-order WAMIT program. The mooring stiffness matrix is obtained from the static offset test. The viscous damping matrix for the hull can also be obtained from the free-decay test. The total mass matrix is obtained by combining platform and wind-turbine weights. Then, the WAMIT is executed again with the new mooring-stiffness matrix and hull viscous damping matrix to obtain platform motions. The second-order wave forces depend on the first-order motions, and in this manner, the second-order difference-frequency wave forces can be calculated more accurately. The hydrodynamic added mass and radiation damping values for the six DOFs of the platform are shown in Fig, 4. As expected, toward the high wave frequency, the added mass converges to a constant value, while radiation damping becomes negligibly small.

7. Wind turbine modeling

The adopted model of 5 MW turbine is the ‘National Renewable Energy Laboratory (NREL) offshore 5 MW baseline wind turbine’. The flexibility of tower is included by using a linear modal representation as suggested in ARTP. Two fore-aft and two side-to-side mode shapes of tower and two flap-wise modes and one edgewise mode of blades are used for coupled dynamic analysis. The natural frequencies of those elastic modes are much higher than the wave and floater-motion frequencies. Tower base is located at the 10 m height from the MWL, so the flexibility of tower begins from that height. The details of the tower-blade-control models can be found in Bae and Kim (2014). It is well known that in the case of semisubmersible-type floater, the flexibility of tower does not play a significant role in overall dynamics especially in the absence of wind.

8. Mooring modeling

The mooring system is composed of equally-spread three catenary lines. The mooring modeling is done by a pre-processor HARP of CHARM3D code. To satisfy the static equilibrium, the total buoyancy of the platform should be the same as the sum of the total structure weight and the vertical-component tension of the mooring system, as shown in Table 3. The high-order finite rod-element method was used for the mooring dynamics modeling, the details of which are given in Kim *et al*. (2001) and Tahar & Kim (2003). The drag coefficient used for the chain mooring was 2.4. The mooring line property is tabulated at Table 2, and the anchor points are tabulated in Table 4.

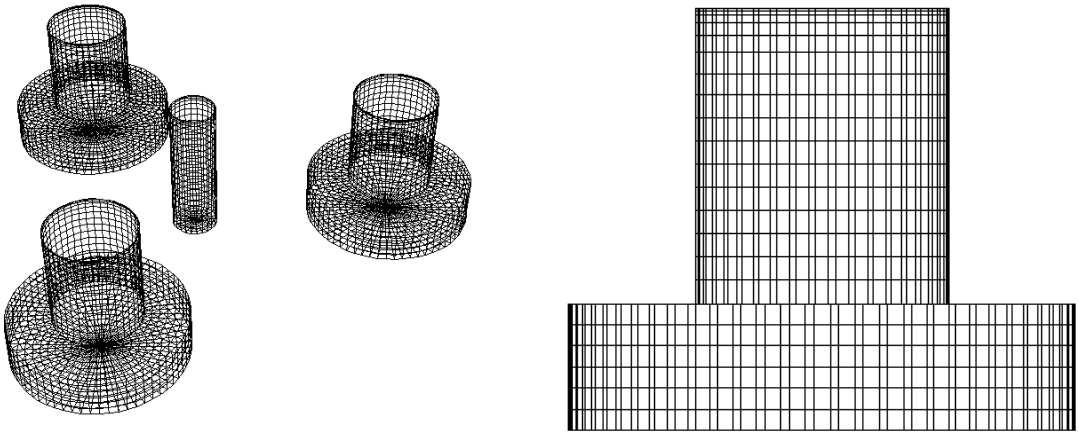

Fig. 3 Numerical Model for potential-flow calculation for OC4 platform

Table 2 Mooring properties

Mooring Type		Chain
Mooring Axial Stiffness	MN	753.6
Unstretched Mooring Line Length	m	835.5
Mooring Mass Density (Dry)	kg/m	113.35
Mooring Mass Density (Wet)	Kg/m	108.63
Seabed Friction Coefficient		1
Mooring Drag Coefficient		2.4
Mooring Added-Mass Coefficient		1

Table 3 vertical-plane static equilibrium

Platform + Tower Weight(N)	1.38703E+08
Buoyancy(N)	1.40589E+08
Total Vertical Tension(N)	1.88612e+06

Table 4 Anchor points

#1 Anchor Point : (418.8, 725.4, -200)
#2 Anchor Point : (-837.6, 0, -200)
#3 Anchor Point : (418.8, -725.4, -200)

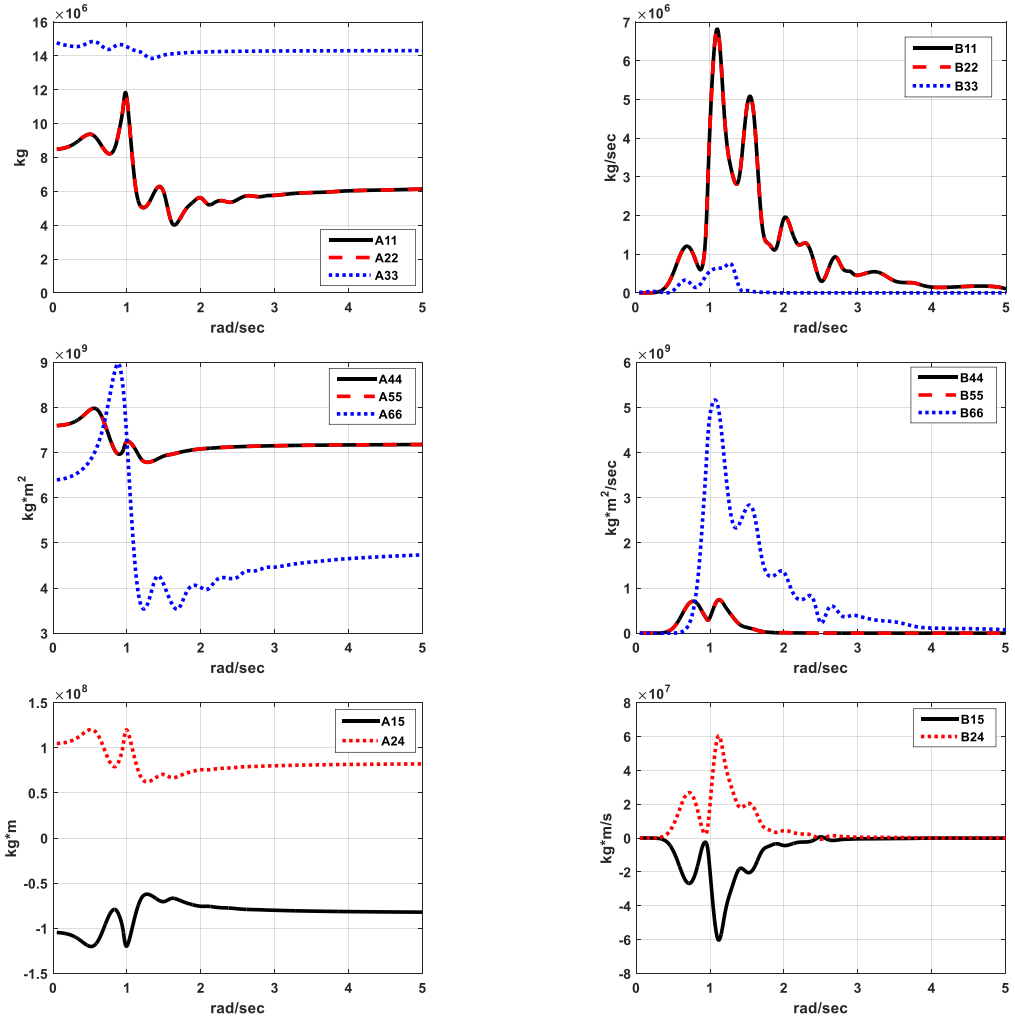

Fig. 4 Hydrodynamic added mass and radiation damping

9. Static offset test

To find the system stiffness, the static offset test for the mooring is numerically done by using FAST-CHARM3D and the relationships between loads and displacements of 6DOFs are shown in Figs. 7-9. The slopes of the curves for heave, roll, and pitch are almost constants because their hydro-static restoring forces are dominant over mooring contributions. However, the slopes for surge and sway increase with displacements showing highly nonlinear hardening behaviors, since it is mostly given by mooring line. The stiffness matrix for small displacements obtained from the static offset is used for WAMIT calculation as an external stiffness in the frequency domain calculations. The total restoring forces in Figs. 7-9 include both hydrostatic and mooring restoring forces. Also, the stiffness of surge and taut/slack side mooring top-tension in the numerical simulation are compared to the model test results in Fig. 6, and they agree very well.

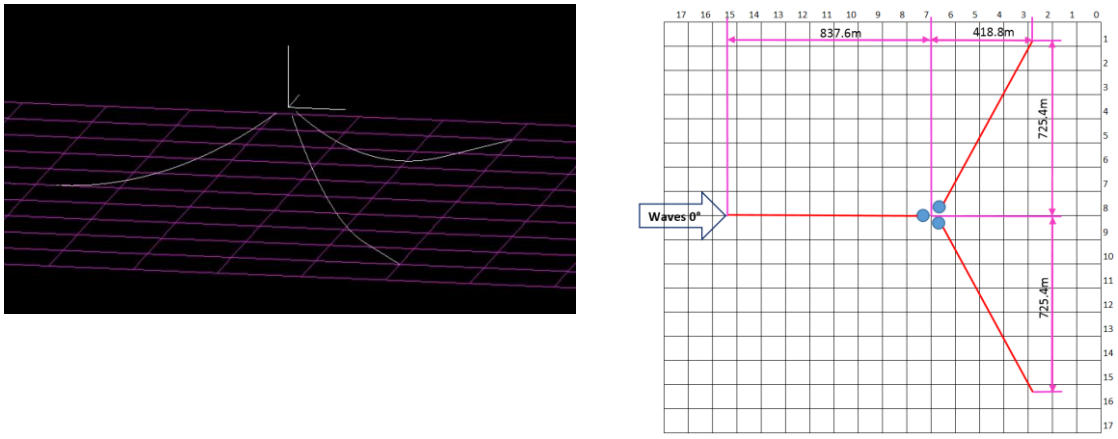

Fig. 5 mooring system modeling by HARP (left) and the mooring arrangement (right)

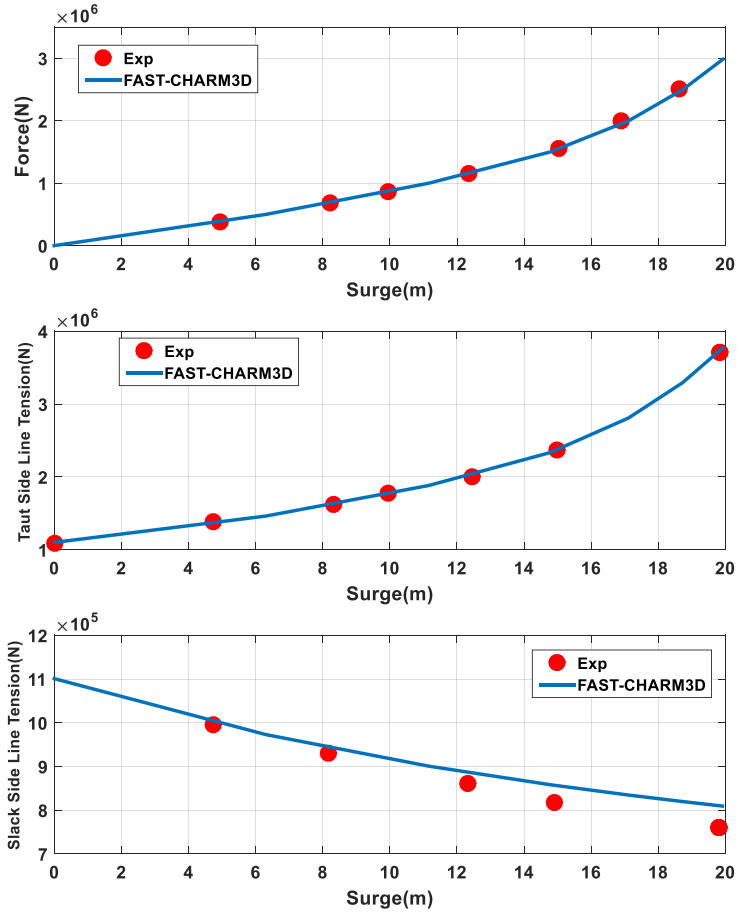

Fig. 6 Comparison of the static offset (Top), taut side line tension (Middle), and slack side line tension(Bottom) between numerical result and measurement data

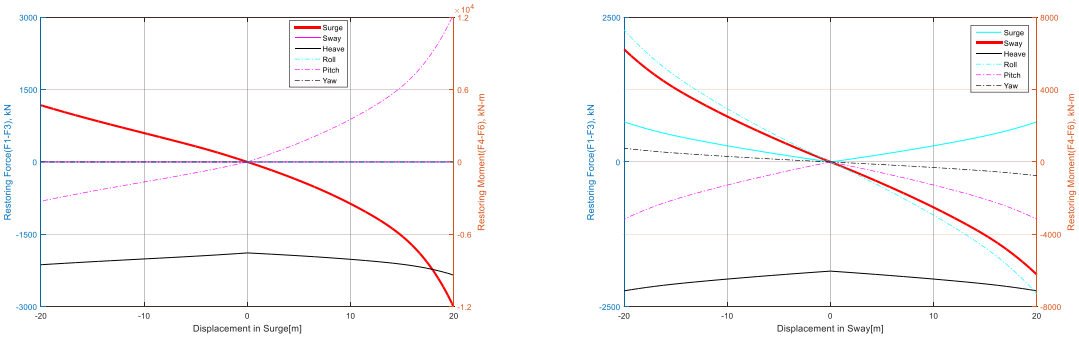

Fig. 7 Load-displacement relationships for the mooring system for surge(left) and sway(right)

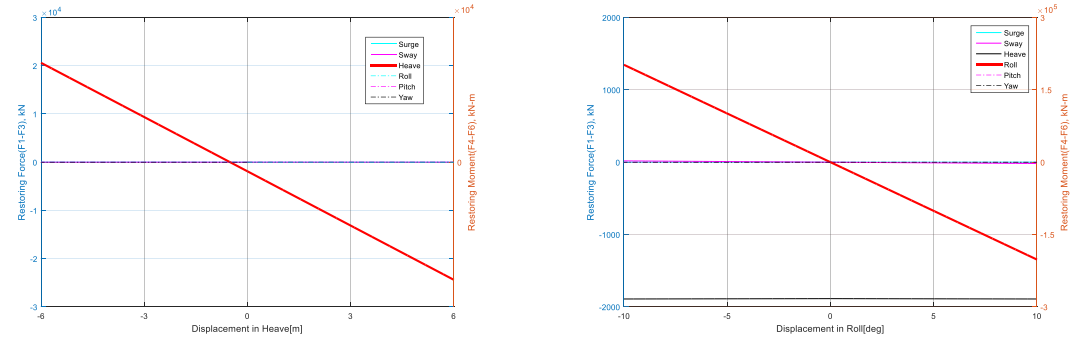

Fig. 8 Load-displacement relationships for the mooring system for Heave (left) and roll (right)

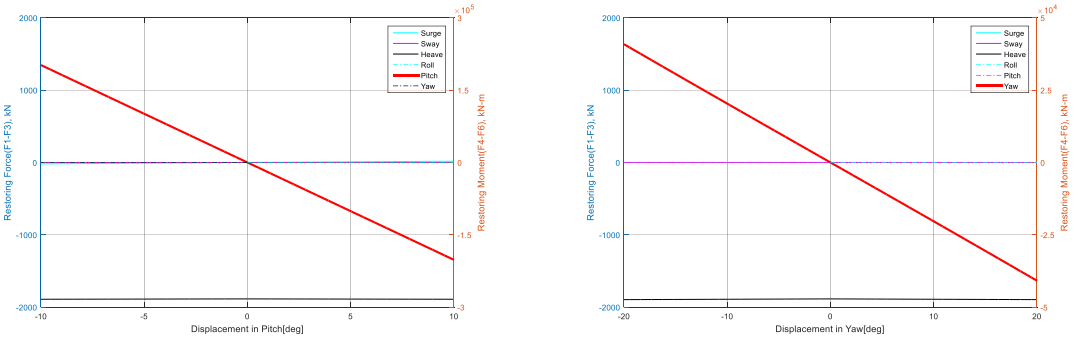

Fig. 9 Load-displacement relationships for the mooring system for pitch (left) and yaw (right)

10. Free-decay test

System natural frequency and damping can be found from free-decay tests. The free-decay test was numerically simulated by FAST-CHARM3D. Various drag coefficients are used to find the appropriate values against experiments. Hull viscous damping for surge mostly comes from the columns. When the column's drag coefficient is 1.6, the simulation results match well against the experimental results. When Cd is zero, only potential-based radiation damping contributes. The majority of heave damping comes from the footings of each column. When its drag coefficient is 3.2, the simulation results agree well with the measurement. The inertia and drag forces on braces are calculated by Morison equation, and added mass coefficient=1.0 and drag coefficient=1.6 are used. The empirical values used in the numerical simulations are tabulated in Table 5. The natural frequencies of the surge and heave simulations are almost the same as the experimental results, as can be seen in Table 6 and Fig. 10. The pitch natural periods of simulation are slightly off compared to the measurements but the difference is small. It may be caused by the slight mismatch of mass distribution and center of gravity, which can easily be produced by inaccurate model fabrication or additional cables in experiment, between the prediction and measurement. It should also be reminded that the added mass can be slightly altered too in the real fluid due to viscous effect. The comparisons of free-decay results between simulation and measurement are plotted in Fig. 10 and the natural frequencies are tabulated in Table 6.

From the free-decay test, system damping ratio can also be obtained. The total-damping ratios are obtained using the concept of logarithmic decrement. The radiation damping ratios are calculated from the same method when drag coefficients are zeros. The viscous damping is obtained by subtracting the radiation damping from the total damping. The respective values are tabulated in Table 7. It is seen that the hull viscous damping plays more important role than the radiation damping and should be included in the motion simulation.

Table 5 Coefficients for Morison member

	Drag Coefficient	Added Mass Coefficient
Column	1.6	N/A (included in radiation model)
Footing	3.2	N/A (included in radiation model)
Brace	1.6	1

Table 6 Natural frequencies

	Natural frequencies(rad/sec)	
DOF	FAST-CHARM3D	Model Test
Surge	0.0556	0.0555
Heave	0.3605	0.3641
Pitch	0.2381	0.2277

Table 7 Damping ratio

	Total Damping	Viscous Damping	Radiation Damping
Surge	12.11%	8.30%	3.81%
Heave	6.66%	5.91%	0.75%
Pitch	6.43%	4.49%	1.94%
Yaw	8.94%	6.91%	2.03%

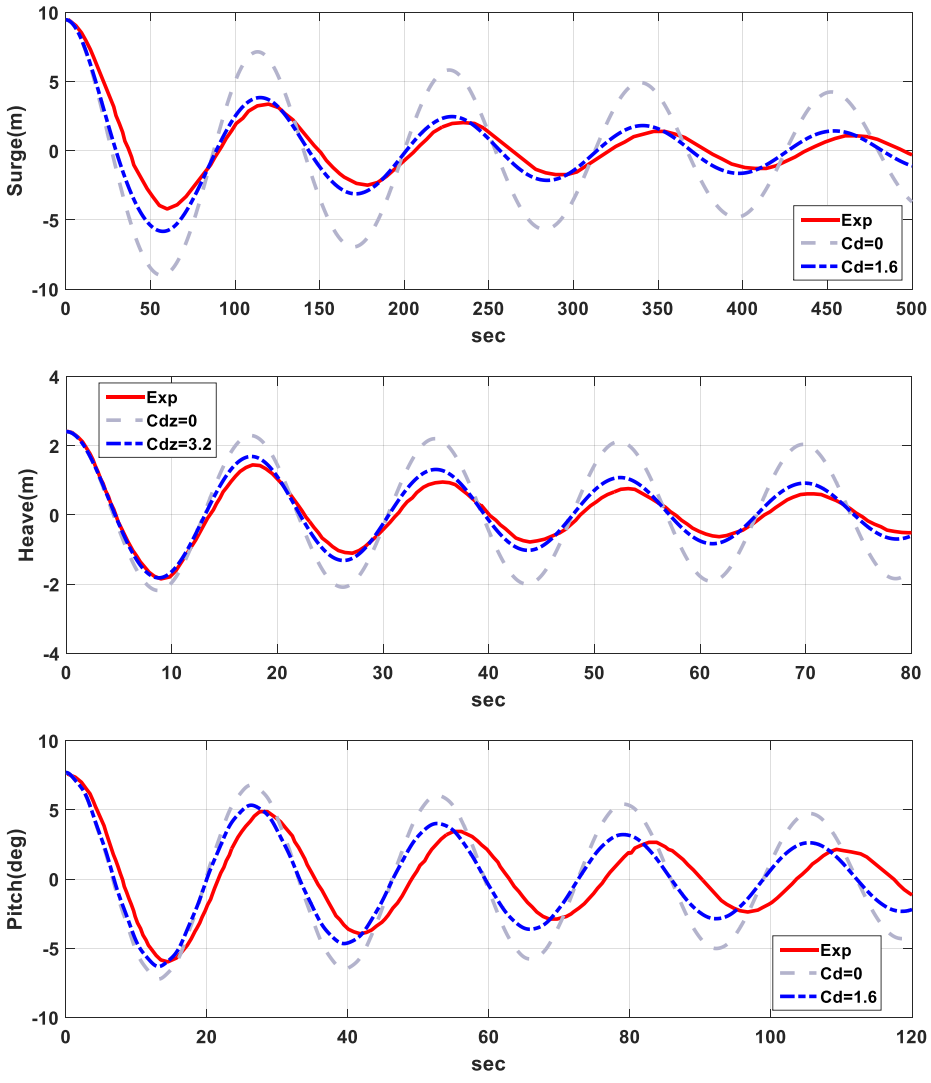

Fig. 10 Surge (Top), Heave (Middle), and Pitch (Bottom) Free decay results

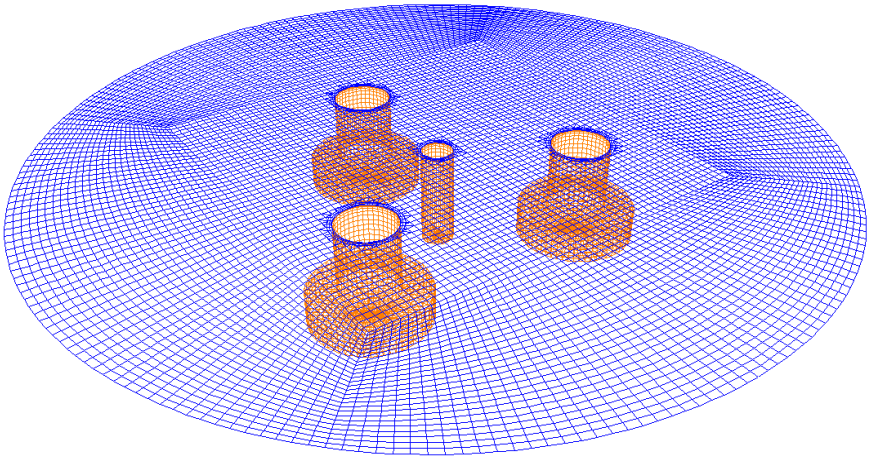

Fig. 11 Free-surface panels for the calculation of second-order wave-force QTFs

11. Second-order diffraction/radiation effects

Since the surge-pitch natural frequencies of the semi-submersible are lower than typical wave frequencies, the second-order difference-frequency wave loadings may play an appreciable role. In this regard, the second-order difference-frequency wave force QTFs (quadratic transfer functions) are calculated by the second-order WAMIT program (e.g., Lee *et al.* 1991). For this, additional free-surface panels are needed. A total of 4888 panels were used for the free surface up to the truncation radius, as can be seen in Fig. 11. The truncation radius of the free-surface circular region is 80 m. The convergence check was also carried out with the increased number of free-surface panels.

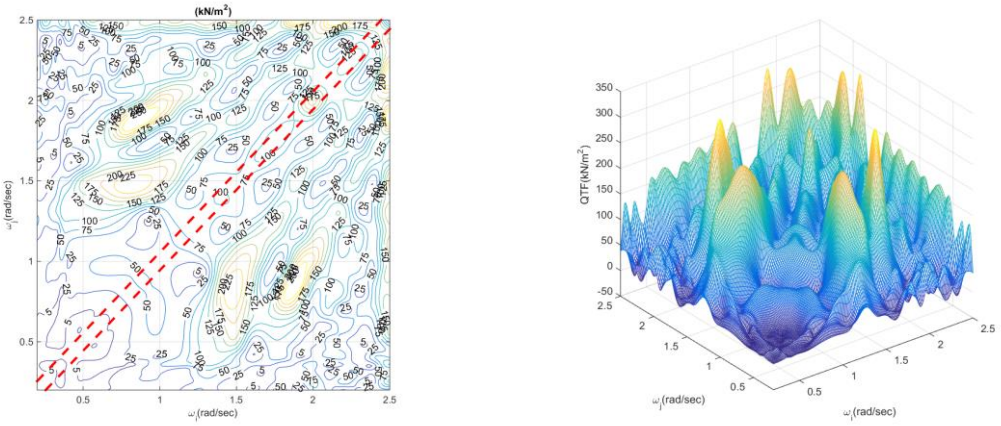

Fig. 12 contour plot (left) and 3d graph (right) of the surge QTF

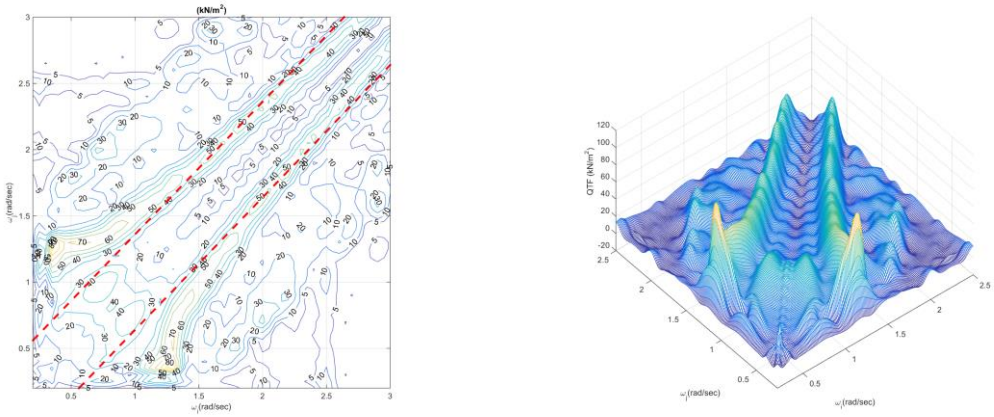

Fig. 13 contour plot (left) and 3d graph (right) of the Heave QTF

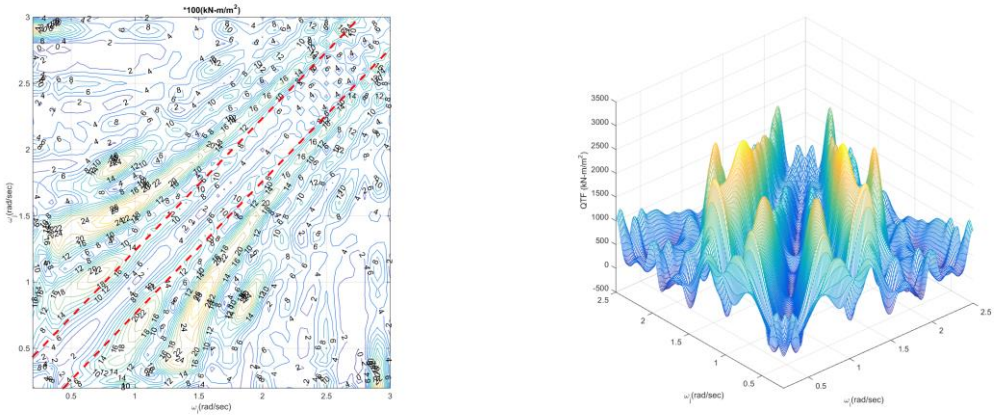

Fig. 14 contour plot (left) and 3d graph (right) of the pitch QTF

The QTF results for all 6DOF are obtained in the bi-frequency domain, as shown in Figs. 12-14, encompassing the typical range of wave frequencies. The QTF values are normalized by bi-chromatic wave amplitudes. The diagonal values represent second-order mean drift forces and moments. The natural frequency line of each DOF motion is displayed as a red dot line. When the natural frequency is very small (close to the diagonal) and the QTF's slope is mild, the so-called Newman's approximation can be used. For example, the surge natural frequency is very small and its QTF slope is relatively mild near the diagonal, so the Newmans' approximation would not be significantly different from the result using the full second-order difference-frequency QTFs. However, it is not necessarily so for the heave and pitch cases. Therefore, we expect appreciable differences between the full-QTF and Newman's approximation results.

12. Case studies

12.1 Wave environments (White-noise wave spectrum)

The same white-noise wave spectra, as in the experiment, are entered into FAST-CHARM3D time-domain simulation program. Then the corresponding irregular waves are generated through FAST-CHARM3D. The low white-noise condition is Hs=7.1 m, T=6~25sec, and the high white-noise condition is Hs=10.5 m, T=6~25sec. 100 wave components were used with the random perturbation of component central frequencies. The comparisons between the regenerated wave spectrum in simulation and the counter-part in measurement are shown in Fig. 15 and the corresponding statistics are tabulated in Table 9. In the low frequency region close to pitch natural frequency, the numerical spectrum value is a little bit smaller than the measured one, which will contribute to minor differences in subsequent results for pitch mode.

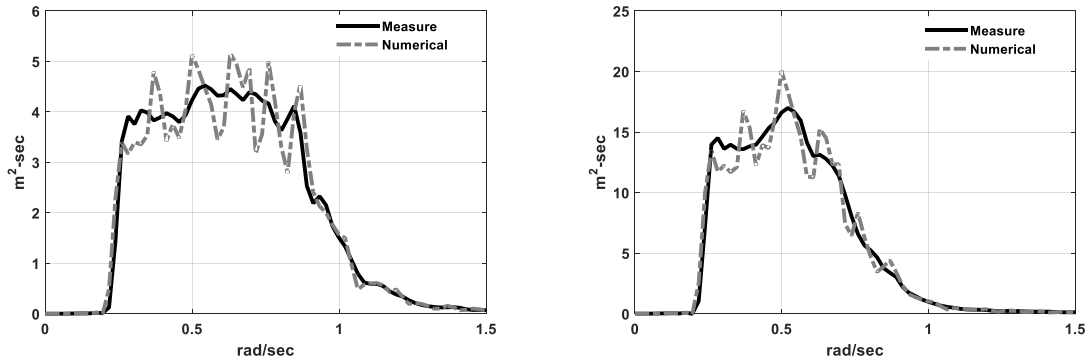

Fig. 15 Low white noise wave spectrum (left) and High white noise wave spectrum (right)

Table 8 White-noise wave condition

	High	Low
Hs	10.5 m	7.1 m
Tp	6~25sec	6~25 sec

Table 9 Generated wave statistics

Wave(m)	White Noise (Low)				White Noise (High)			
	Max	Min	Mean	Std	Max	Min	Mean	Std
Exp	7.841	-6.691	-0.018	1.755	12.814	-11.008	-0.034	2.853
Sim	6.179	-6.836	0	1.755	10.03	-11.64	0	2.845

13. Simulation results and discussions

So far, we checked that all the dynamic system characteristics and wave environments are modeled correctly so that we can produce various kinds of performance simulation results. We first selected two white-noise wave conditions as shown in Fig. 15. The white-noise wave spectrum is a kind of artificial one but it is more useful in checking the correct modeling of a dynamic system since the input energy is uniformly distributed for relevant frequency range. As discussed earlier, the drag coefficient of 1.6 for columns and 3.2 for footings were selected from the free-decay test in calm water. In the wave environments, the drag coefficients may be slightly altered. The forces on Morison members are evaluated at the instantaneous body position and up to the instantaneous free-surface elevation with the Morison's formula for a moving body. The wave particle kinematics above MWL are generated by using a uniform extrapolation technique. As discussed earlier, to include the second-order wave diffraction effect, both Newman's approximation and full-QTF method are used. The results are also compared against a separate result excluding the second-order diffraction effects i.e. with including only the first-order wave forces and moments.

The surge, heave, pitch, and mooring top tension time-series and their spectra are shown in Figs. 16-23 for both high and low white-noise input wave spectra. When the full second-order wave force is added, the numerical results best match against the experimental results. When only first-order wave forces are used, surge and pitch slowly varying motions are significantly underestimated, while there is no appreciable difference in heave motion. The underestimation of surge and pitch slowly varying motions directly affects the same trend for mooring-line tension. In case of surge, the slowly varying motions are dominant over the wave-frequency motions. The overall trend is very similar between low and high input spectrum cases. If the range of input white-noise spectra does not include the pitch natural frequency, the error associated with the linear-wave-force-only case is to be greatly increased. The Newman's approximation is generally good for slowly varying surge motions, but less accurate for slowly varying pitch motions due to the reason discussed earlier. In case of heave mode, the first-order wave forces are dominant over second-order contributions, so all the 3 cases give almost identical numerical results. The overall reproduceability of the experimental results by the present numerical method is significantly improved compared to prior attempts (e.g., Masciola *et al*. 2013, Coulling *et al*. 2013a, b).

To more clearly explain the above phenomena, the second-order difference-frequency wave-force spectra are plotted in Fig. 24 for both Newman's approximation and full QTF cases. The numerically regenerated spectra are also compared with theoretical ones by using the following formulas for full QTF (Eq. (8)) (Kim and Yue 1990) and for Newman's approximation (Eq. (9)) (Pinkster 1975, Faltisen 2012).

$$S_F(\mu) = 8\int_0^\infty S(\omega+\mu)S(\omega)\left|T_{jk}(\omega+\mu,\omega)\right|^2 d\omega \tag{8}$$

$$S_F(\mu)_{newman} = 8\int_0^\infty S(\omega+\mu)S(\omega)\left|T_{jj}(\omega+\mu/2\,)\right|^2 d\omega \tag{9}$$

Where $S(\omega)$ is the input wave spectrum, T_{jk}, T_{jj} are the QTF components.

The numerically regenerated second-order difference-frequency wave-force spectra agree well with the theoretical ones, which double checks that all the simulated results are correct. In case of surge mode, there is significant difference between the Newman's approximation and full-QTF cases in higher frequencies but they are close near the location of surge natural frequency. It is the

reason why the Newman's approximation does pretty good job for predicting slowly varying surge motions. In case of pitch mode, there is significant difference between the Newman's approximation and full-QTF cases even near the pitch natural frequency, so the Newman's approximation method does worse job compared to the surge case. The overall trend is similar between the low and high input spectra.

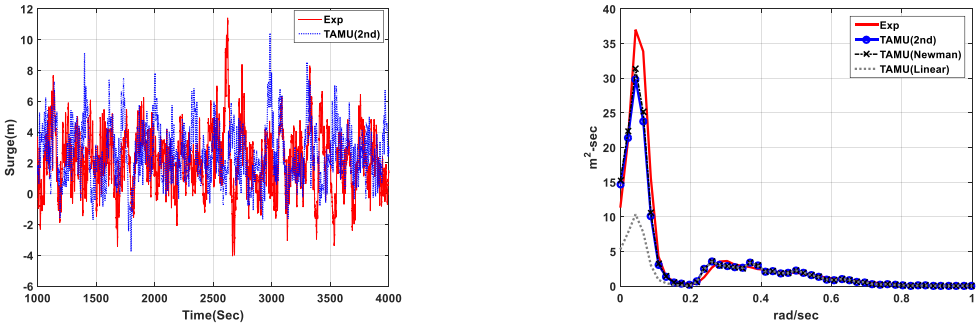

Fig. 16 surge time series (left) and spectrum (right) in the low white noise spectrum

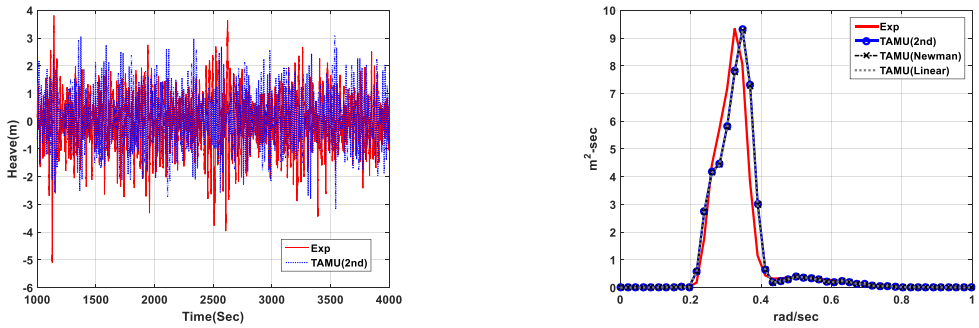

Fig. 17 heave time series (left) and spectrum (right) in the low white noise spectrum

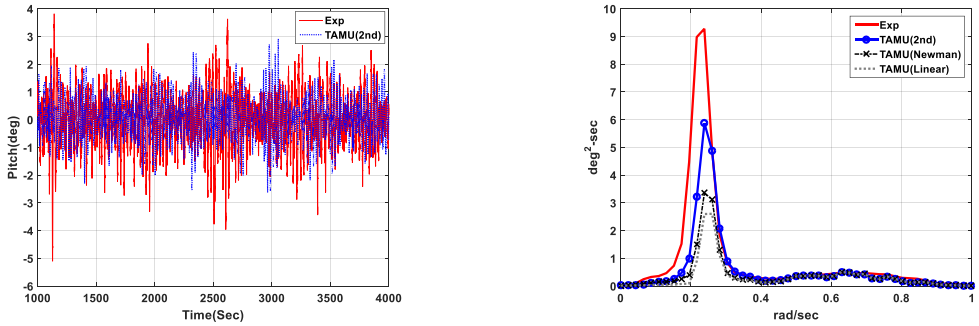

Fig. 18 pitch time series (left) and spectrum (right) in the low white noise spectrum

In the case of time series, only the full-QTF case is compared against experimental data to avoid the confusion of too many lines co-existing. The initial transient parts of the time series were eliminated for more accurate steady-state statistical values. The numerical simulations generally reproduce the key trends of physical experiments even for the mooring-line dynamics. The statistics of those responses in high and low input-wave-spectrum cases are tabulated in Table 10.

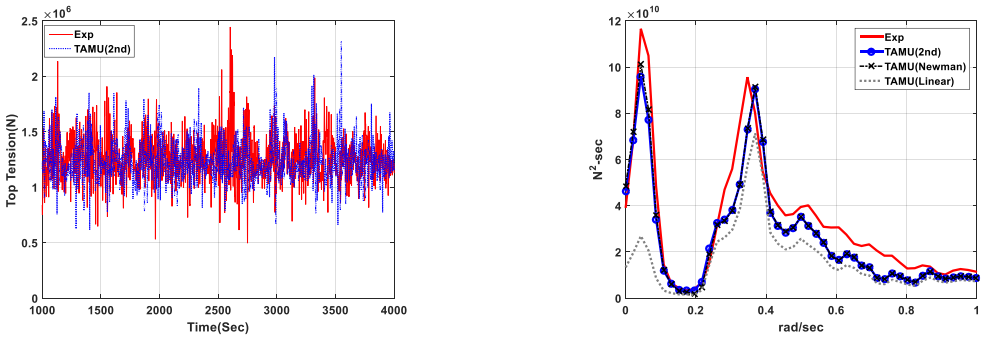

Fig. 19 mooring top tension time series (left) and spectrum (right) in the low white noise spectrum

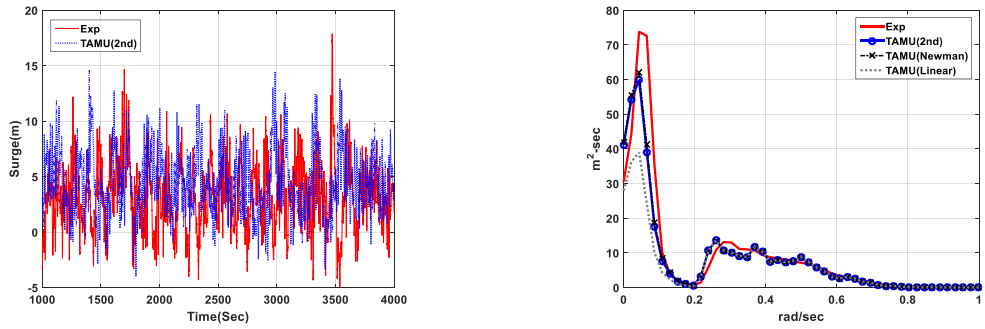

Fig. 20 surge time series (left) and spectrum (right) in the high white noise spectrum

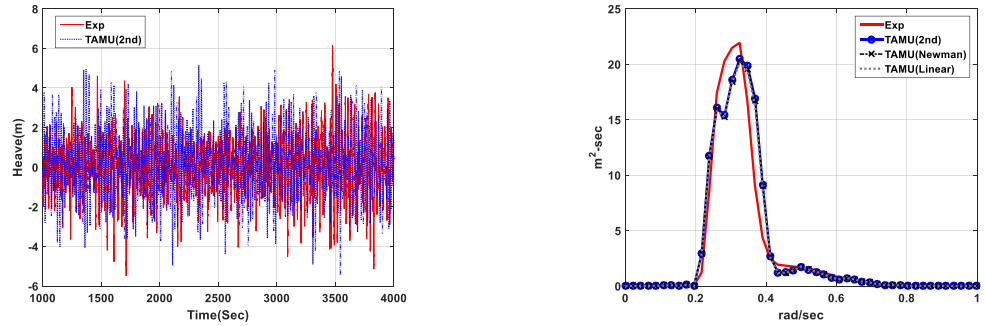

Fig. 21 heave time series (left) and spectrum (right) in the high white noise spectrum

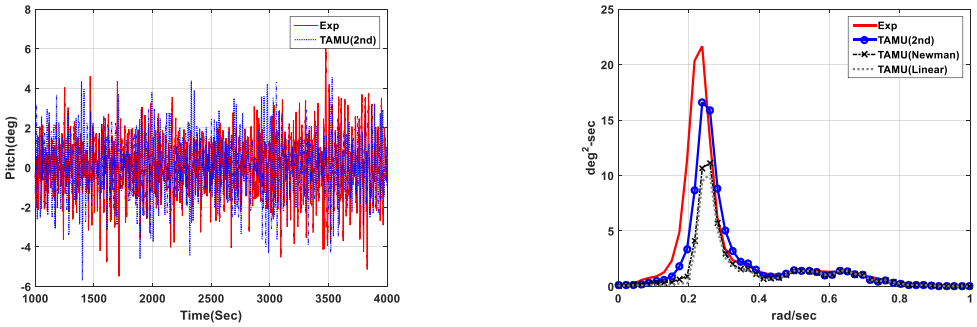

Fig. 22 pitch time series (left) and spectrum (right) in the high white noise spectrum

Table 10 Surge, Heave, Pitch and Top tension statistics of high and low white noise spectra

		WhiteNoise (High)				WhiteNoise (Low)			
		Max	Min	Mean	Std	Max	Min	Mean	Std
Surge (m)	Exp	17.878	-5.008	3.402	3.034	11.420	-4.918	2.169	1.900
	second	14.631	-4.793	4.496	2.828	10.424	-3.752	2.547	1.769
	Newman	15.408	-5.001	4.544	2.859	10.376	-3.829	2.579	1.797
	Linear	12.321	-5.182	2.893	2.529	6.893	-3.211	1.234	1.313
Heave (m)	Exp	5.993	-6.399	0.043	1.739	3.396	-3.445	-0.044	1.002
	second	5.825	-5.697	0.169	1.788	3.394	-3.363	0.121	1.036
	Newman	5.845	-5.802	0.165	1.780	3.389	-3.413	0.119	1.034
	Linear	5.415	-6.005	0.073	1.770	3.232	-3.474	0.079	1.031
Pitch (deg)	Exp	6.465	-7.243	0.060	1.594	3.819	-5.106	-0.069	0.984
	second	5.185	-5.957	0.120	1.406	3.130	-3.043	0.071	0.772
	Newman	4.624	-4.578	0.113	1.165	2.630	-2.347	0.067	0.635
	Linear	4.192	-4.448	-0.016	1.106	1.995	-2.340	0.005	0.579
Top Tension (MN)	Exp	5.867	0.039	1.348	0.488	2.445	0.429	1.267	0.185
	second	4.032	-0.039	1.352	0.445	2.497	0.388	1.233	0.166
	Newman	4.077	-0.050	1.357	0.447	2.560	0.432	1.236	0.167
	Linear	3.391	-0.064	1.248	0.385	2.133	0.336	1.160	0.133

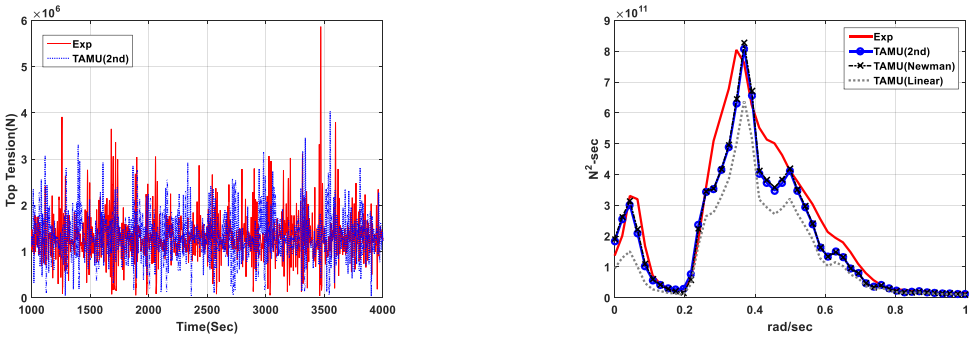

Fig. 23 mooring top tension time series (left) and spectrum (right) in the high white noise spectrum

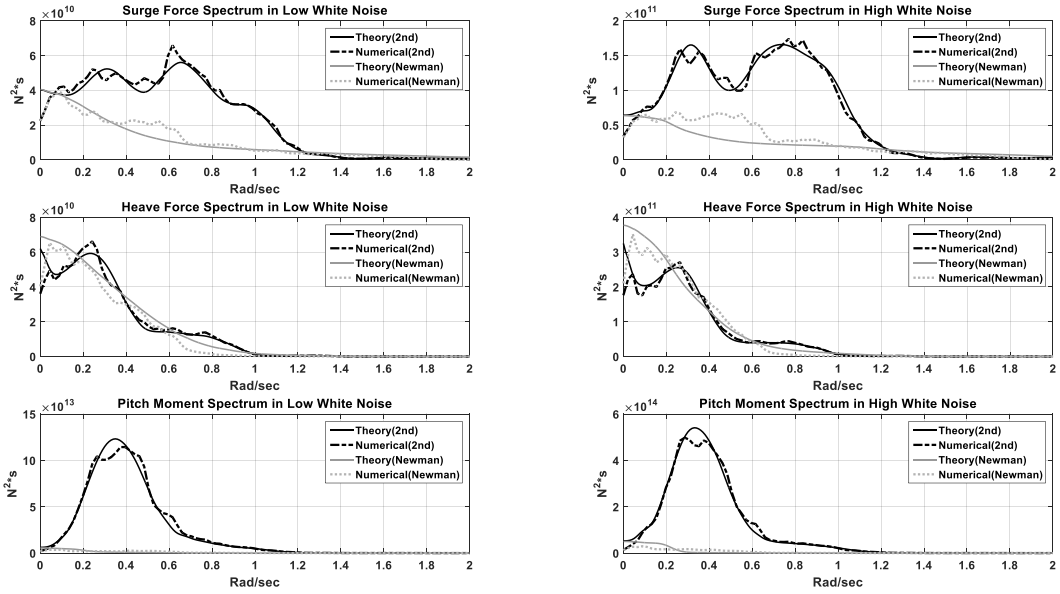

Fig. 24 Comparison of second-order-diffraction force/moment spectra between numerical and theoretical results in low (left) and high (right) white noise spectrum

14. Conclusions

The global performance of the 5 MW OC4 semisubmersible floating wind turbine was numerically simulated by using the turbine-floater-mooring fully coupled dynamic analysis program FAST-CHARM3D in time domain. The numerical static-offset and free-decay tests were conducted after dynamic-system modeling to verify the system stiffness, damping, and natural frequencies compared with DeepCWind experimental results. The potential-theory-based first- and second-order hydrodynamics results including complete QTFs were calculated through WAMIT in the frequency domain, which were subsequently used in the time-domain simulations. In the case of random waves, two white-noise input spectra representing high and low seas were used. To

investigate second-order wave diffraction effects, both Newman's approximation and full-QTF method were used for comparison. The results were also compared against the corresponding experiments and a separate simulation result excluding all the second-order diffraction effects i.e. with including only the first-order wave forces and moments.

If the second-order difference-frequency force/moment is excluded, the surge, pitch, and mooring top tension are significantly under-estimated compared to the experimental results but heave is not much affected by the second-order wave-diffraction effects. When the complete second-order full QTF is used, the simulated time series and spectra for surge-heave-pitch motions and mooring tensions best match against the corresponding experimental results. For the given case, Newman's approximation works well for slowly varying surge motions but appreciably underestimates the slowly varying pitch motions since the pitch natural frequency is not so small. The regenerated second-order slowly varying force/moment spectra from the corresponding time series data also agree well with the theoretical values, which confirms that all the simulation results including second-order diffraction effects are done in a reliable manner. The corresponding statistical values for floater motions and mooring tensions also correlate well against experimental values, which clearly demonstrates that the present simulation method with full QTF can be a useful tool for the design of semi-submersible-type floating wind turbine.

Acknowledgments

The present work is a result of the project "Development of the design technologies for a 10MW class wave and offshore wind hybrid power generation system" granted by the Korea Ministry of Oceans and Fisheries. It is also partially supported by POSCO and ABS.

References

Bae, Y.H. and Kim, M.H. (2011), "Rotor-floater-mooring coupled dynamic analysis of mono-column-TLP-type FOWT (Floating Offshore Wind Turbine)", *Ocean Syst. Eng*., **1**(1), 93-109.

Bae, Y.H. and Kim, M.H. (2014), "Coupled dynamic analysis of multiple wind turbines on a large single floater", *J. Ocean Eng*., **92**, 175-187.

Coulling, A.J., Goupee, A.J., Robertson, A.N., Jonkman, J.M. and Dagher, H.J. (2013), "Validation of a FAST semi-submersible floating wind turbine numerical model with DeepCwind test data", *J. Renew. Sust. Energy*, **5**(2).

Bae, Y.H. and Kim, M.H. (2014), "Influence of control strategy to FOWT global performance by aero-elastic-control-floater-mooring coupled dynamic analysis", *J. Ocean Wind Energy*, **1**(1), 50-58.

Coulling, A.J., Goupee, A.J., Robertson, A.N. and Jonkman, J.M. (2013), "Importance of second-order difference-frequency wave-diffraction forces in the validation of a fast semi-submersible floating wind turbine model", *Proceedings of the 32th (2013) International Conference on Ocean, Offshore and Arctic Engineering Nantes*, France.

Dominique, R., Christian, C., Alexia, A. and Alla, W. (2010), "WindFloat: A floating foundation for offshore wind turbines", *J. Renew. Sust. Energy*, **2**(3),

Faltisen, O.M. (2012), Sea loads on ships and offshore structures, Cambridge University Press, 158-159.

Henderson, A.R., Leutz, R. and Fujii, T. (2002), "Potential for floating offshore wind energy in Japanese waters", *Proceedings of the 12th (2002) International Offshore and Polar Engineering Conference*, Kitakyushu, Japan.

Henderson, A.R., Zaaijer, M., Bulder, B., Pierik, J., Huijsmans, R., Van Hees, M., Snijders, E., Wijnants,

G.H. and Wolf, M.J. (2004), "Floating windfarms for shallow offshore sites", *Proceedings of the 14th (2004) International Offshore and Polar Engineering Conference*, Toulon, France.
Jonkman, J.M. and Buhl Jr, M.L. (2004), *FAST user's guide. National Renewable Energy Laboratory*, Rept. NREL/EL-500–29798, Golden, Colorado.
Jonkman, J.M., Butterfield, S., Musial, W. and Scott, G. (2007), *Definition of a 5-MW Reference Wind Turbine for Offshore System Development*, NREL Technical Report No. TP-500-38060.
Kang, H.Y. and Kim, M.H. (2012), "Hydrodynamic interactions and coupled dynamics between a container ship and multiple mobile harbors", *Ocean Syst. Eng*., **2**(3), 217-228.
Kim, M.H. and Yue, D.K.P. (1991), "Sum- and difference-frequency wave loads on a body in unidirectional Gaussian seas", *J. Ship Res.*, **35**, 127-140.
Kim, M.H. and Yue, D.K.P. (1989), "The complete second-order diffraction solution for an axisymmetric body. Part 1. Monochromatic incident waves", *J. Fluid Mech.*, **200**, 235-264.
Kim, M.H. and Yue, D.K.P. (1990), "The complete second-order diffraction solution for an axisymmetric body. Part 2. Bichromatic incident waves and body motions", *J. Fluid Mech.*, **211**, 557-593, 1990.
Kim, M.H., Ran, Z. and Zheng, W. (2001), "Hull/mooring coupled dynamic analysis of a truss spar in time domain", *Int. J. Offshore Polar*, **11**(1), 42-54.
Koo, B.J., Goupee, A.J., Kimball, R.W. and Lambrakos, K.F. (2014a), "Model tests for a floating wind turbine on three different floaters", *J. Offshore Mech. Arct.*, **136**(2), 021904.
Koo, B.J., Goupee, A.J., Lambrakos, K. and Lim, H.J. (2014b), "Model test data correlations with fully coupled hull/mooring analysis for a floating wind turbine on a semi-submersible platform", *Proceedings of the 33th (2014) International Conference on Ocean, Offshore and Arctic Engineering*, San Francisco, USA.
Lee, C.H., Newman, J.N., Kim, M.H. and Yue, D.K.P. (1991), "The computation of second-order wave loads", *Proceedings of the 10th Offshore Mechanics and Artic Eng. Conference*, Stavanger, Norway.
Masciola, M., Robertson, A.N., Jonkman, J.M., Alexander Coulling, A.J. and Goupee, A.J. (2013), "Assessment of the importance of mooring dynamics on the global response of the DeepCWind floating semisubmersible offshore wind turbine", *The International Society of Offshore and Polar Engineers.*
Musial, W.D., Butterfield, S. and Boone, A. (2004), "Feasibility of floating platform systems for wind turbines", Paper presented at the 4second AIAA Aerospace Sciences Meeting and Exhibit, Reno, NV.
Pinkster, J.A. (1975), "Low-frequency phenomena associated with vessels moored at sea", *Soc. Petroleum Engineers J.*, December, 487-494.
Tahar, A. and Kim, M.H. (2003), "Hull/mooring/riser coupled dynamic analysis and sensitivity study of a tanker-based FPSO", *J. Appl. Ocean Res*., **25**(6), 367-382.
Tong, K.C. (1998), "Technical and economic aspects of a floating offshore wind farm", *J. Wind Eng. Ind. Aerod*., **74-76**, 399-410.
Wayman, E.N., Sclavounos, P.D., Butterfield, S., Jonkman, J. and Musial, W. (2006), "Coupled dynamic modeling of floating wind turbine systems", *Proceedings of the Offshore Technology Conference*, Houston, TX.
Wenchao, Z. and Deeheng, W. (2015), "Numerical study of interactions between phase II of OC4 wind turbine and its semi-submersible floating support system", *J. Ocean Wind Energy*, **2**(1), 45-53.
Yang, C.K. and Kim, M.H. (2010), "Transient effects of tendon disconnection of a TLP by hull-tendon-riser coupled dynamic analysis", *J. Ocean Eng*., **8-9**, 667-677.